

Constraining the ^{13}C neutron source in AGB stars through isotopic analysis of trace elements in presolar SiC

J. G. BARZYK^{1, 2, 3†*}, M. R. SAVINA^{2, 3}, A. M. DAVIS^{1, 3, 4}, R. GALLINO^{5, 6}, F. GYNGARD⁷, S. AMARI⁷,
E. ZINNER⁷, M. J. PELLIN^{2, 3}, R. S. LEWIS^{3, 4}, and R. N. CLAYTON^{1, 3, 4, 8}

¹Department of the Geophysical Sciences, University of Chicago, Chicago, Illinois 60637, USA

²Materials Science Division, Argonne National Laboratory, Argonne, Illinois 60439, USA

³Chicago Center for Cosmochemistry, Chicago, Illinois 60637, USA

⁴Enrico Fermi Institute, University of Chicago, Chicago, Illinois 60637, USA

⁵Dipartimento di Fisica Generale, Università di Torino, 10125 Torino, Italy

⁶Center for Stellar and Planetary Astrophysics, School of Mathematical Sciences, Monash University, Victoria 3800, Australia

⁷Laboratory for Space Sciences and the Physics Department, Washington University, Saint Louis, Missouri 63130, USA

⁸Department of Chemistry, University of Chicago, Chicago, Illinois 60637, USA

[†]Present address: U.S. Environmental Protection Agency, National Homeland Security Research Center,
Research Triangle Park, North Carolina 27711, USA

*Corresponding author. E-mail address: barzyk.julia@epa.gov

(Received 13 November 2006; revision accepted 17 April 2007)

Abstract—Analyses of the isotopic compositions of multiple elements (Mo, Zr, and Ba) in individual mainstream presolar SiC grains were done by resonant ionization mass spectrometry (RIMS). While most heavy element compositions were consistent with model predictions for the slow neutron capture process (*s*-process) in low-mass (1.5–3 M_{\odot}) asymptotic giant branch stars of solar metallicity when viewed on single-element three-isotope plots, grains with compositions deviating from model predictions were identified on multi-element plots. These grains have compositions that cannot result from any neutron capture process but can be explained by contamination in some elements with solar system material. Previous work in which only one heavy element per grain was examined has been unable to identify contaminated grains. The multi-element analyses of this study detected contaminated grains which were subsequently eliminated from consideration. The uncontaminated grains form a data set with a greatly reduced spread on the three-isotope plots of each element measured, corresponding to a smaller range of ^{13}C pocket efficiencies in parent AGB stars. Furthermore, due to this reduced spread, the nature of the stellar starting material, previously interpreted as having solar isotopic composition, is uncertain. The constraint on ^{13}C pocket efficiencies in parent stars of these grains may help uncover the mechanism responsible for formation of ^{13}C , the primary neutron source for *s*-process nucleosynthesis in low-mass stars.

INTRODUCTION

Isotopic compositions of heavy elements that are present in trace abundances in presolar grains provide information about stars that cannot be obtained from astronomical observation. The majority (~90%) of presolar SiC grains, called “mainstream” (Zinner 1998), carry the signature of the slow neutron capture process (*s*-process) and originate in the outflows of carbon-rich asymptotic giant branch (AGB) stars of low mass (1.5 to 3 M_{\odot}) and of close to solar metallicity (Gallino et al. 1998; Lugaro et al. 2003a). They have $^{12}\text{C}/^{13}\text{C}$ ratios between 10 and 100, matching those of AGB stars (Anders and Zinner 1993), $^{14}\text{N}/^{15}\text{N}$ ratios between 200 and

20,000, and ($^{29}\text{Si}/^{28}\text{Si}$) and ($^{30}\text{Si}/^{28}\text{Si}$) values between –50 and +200 (Zinner 1998) in δ -notation, where δ represents the permil deviation of an isotopic ratio with respect to solar:

$$\delta\left(\frac{aX}{bX}\right)(\text{‰}) = \left[\frac{\left(\frac{aX}{bX}\right)_{\text{grain}}}{\left(\frac{aX}{bX}\right)_{\text{standard}}} - 1 \right] \times 1000 \quad (1)$$

Because our focus is on the *s*-process occurring in AGB stars, this study considers mainstream grains only. Type A, B,

X, Y, and Z grains will be considered elsewhere. Type Y and Z grains, which are also believed to come from AGB stars, originate in AGB stars with less-than-solar metallicity (Hoppe et al. 1997; Zinner et al. 2006).

Stellar nucleosynthesis models indicate that the amount of ^{13}C available to drive the $^{13}\text{C}(\alpha, n)^{16}\text{O}$ reaction controls the magnitude of the *s*-process signature in presolar grains. Carbon-13 is thought to form in a “pocket” at H re-ignition; later on it will undergo alpha capture, releasing neutrons in radiative conditions before the development of the next convective instability. This pocket becomes the site of *s*-process nucleosynthesis, and its size controls the magnitude of neutron exposure experienced by seed nuclei. This ^{13}C quantity has been referred to as the ^{13}C pocket efficiency. Previous studies of single presolar SiC grains have attempted to constrain the ^{13}C pocket efficiency by measuring the isotopic compositions of heavy elements, including Mo (Nicolussi et al. 1998b), Zr (Nicolussi et al. 1997), Sr (Nicolussi et al. 1998d), Ba (Savina et al. 2003a), and Ru (Savina et al. 2004). These studies led to the conclusion that presolar grains contain trace elements synthesized under a wide range of ^{13}C pocket efficiencies in AGB stars of low mass ($1.5\text{--}2\text{ }M_{\odot}$) where the neutron exposure due to the minor $^{22}\text{Ne}(\alpha, n)^{25}\text{Mg}$ neutron source is weak (Lugaro et al. 2003a).

When interpreting isotopic compositions of presolar grains, it is crucial that the grains are representative samples of their parent stars. A grain condenses from stellar ejecta, is incorporated into a meteorite in the early solar system, travels to Earth, and is separated from the meteorite and prepared for analysis. It inevitably comes into contact with material not from the parent star, and therefore the potential for contamination exists. It is thus desirable to identify such contamination when it exists. This study presents data on multiple heavy elements in single presolar SiC grains—something previously done for only a small number of presolar graphite grains (Nicolussi et al. 1998a, 1998c). This allows us to identify grains whose compositions are not representative of parent star compositions. When only grains that are apparently free of contamination are considered, we find that we can place constraints on the range of ^{13}C pocket efficiencies.

In the Methods section, we describe how the grains were imaged by scanning electron microscopy (SEM) and analyzed by resonant ionization mass spectrometry (RIMS) and secondary ionization mass spectrometry (SIMS). In the Results section, we present the C, N, Si, Mo, Zr, and Ba isotopic data for the grains. In the Discussion section, we describe how isotopically unusual mainstream grains were identified, how they may have been contaminated with terrestrial material, and how the remaining data can be used to constrain ^{13}C pocket efficiencies, along with other astrophysical interpretations. The findings are summarized and implications discussed in the Conclusions section.

THEORETICAL BACKGROUND

Recent reviews of AGB stellar evolution and nucleosynthesis are given by Busso et al. (1999) and Herwig (2005). An overview is given by Lugaro (2005). AGB stars consist of a C-O core, He-burning and H-burning shells, a He-rich intershell and a H-rich envelope. They experience recurrent thermal pulses (thermonuclear runaway resulting from He-burning and associated local temperature increase) that cause the He-intershell region to become convective for a brief period. Convection causes the products of partial He-burning to be mixed throughout the entire He-intershell. The star expands in response to a thermal pulse, resulting in a reduction of temperature and density of the outer layers of the H-burning zone just below the envelope and in the temporary inactivation of the H shell. About 1000 years after the quenching of a convective thermal pulse, the convective envelope extends below the inactivated H-shell into the outer region of the He-intershell, thus mixing the contents of the envelope with fresh nucleosynthesis products, including ^{12}C and *s*-process isotopes. This is referred to as a third dredge-up. The amount of He-intershell material involved in each third dredge-up varies with pulse number. We follow the stellar evolutionary prescriptions of Straniero et al. (2006).

s-Process Neutron Sources and Exposure

The $^{13}\text{C}(\alpha, n)^{16}\text{O}$ reaction is the major neutron source for *s*-process nucleosynthesis in AGB stars. Carbon-13 is assumed to form by diffusion of small amounts of protons from the envelope into the top layers of the ^{12}C -rich He-intershell during a third dredge-up event, followed at H reignition by proton capture on the abundant ^{12}C through the chain $^{12}\text{C}(p, \gamma)^{13}\text{N}(\beta^+\nu)^{13}\text{C}$. This thin region is known as the “ ^{13}C pocket.” Later, when the temperature of the pocket reaches about $0.9 \times 10^8\text{ K}$, all ^{13}C nuclei are consumed by the reaction $^{13}\text{C}(\alpha, n)^{16}\text{O}$ over a few thousand years in the radiative conditions of the interpulse phase. The $^{13}\text{C}(\alpha, n)^{16}\text{O}$ reaction generates low neutron densities ($N_n \leq 10^7\text{ cm}^{-3}$), but a large time-integrated neutron flux (neutron exposure).

Neutron capture on seed nuclei makes the pocket highly enriched in *s*-process elements. The pocket is subsequently engulfed by the next convective thermal instability and the *s*-process elements are diluted over the entire He-intershell.

A minor neutron source is driven by marginal activation of the $^{22}\text{Ne}(\alpha, n)^{25}\text{Mg}$ reaction during late thermal pulses. In low-mass AGB stars the maximum temperature at the bottom of the convective shell increases slightly with pulse number up to $\sim 3 \times 10^8\text{ K}$. A neutron burst of short duration but with a high neutron peak density of up to 10^{10} cm^{-3} is released. In these conditions, while the neutron exposure is very small, a number of “branchings” are open along the *s*-path at unstable nuclei, where the neutron capture channel may compete with β -decay. This is illustrated in Fig. 1 where, at the low neutron

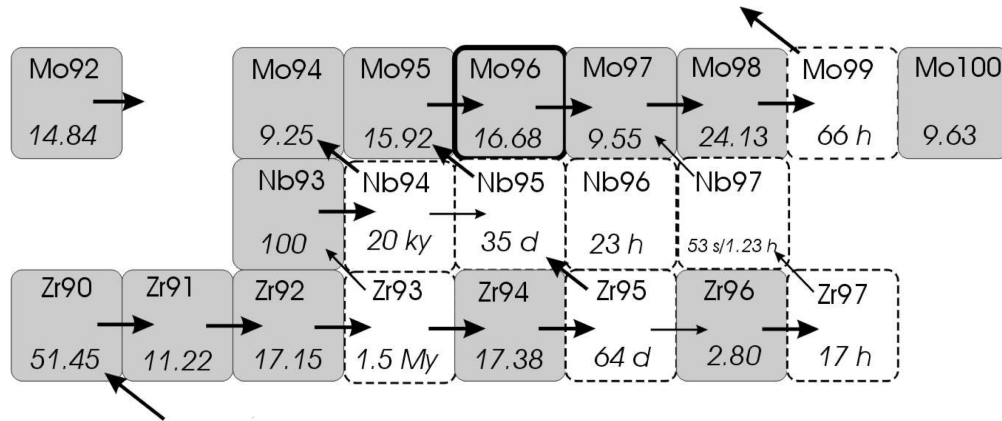


Fig. 1. The Zr to Mo section of the chart of the nuclides. The main path of the *s*-process is shown with thick arrows. Alternative paths are indicated with thin arrows. Stable nuclides are dark gray and unstable nuclides are white. Abundances in percent are shown for the stable and half-lives for the unstable nuclides.

flux released by the ^{13}C source, nucleosynthesis proceeds along the main path as shown by the thick arrows, with unstable nuclides such as ^{95}Zr and ^{95}Nb decaying before they can capture neutrons. At the higher neutron flux released by the ^{22}Ne source, the neutron channel on ^{95}Zr competes with β -decay, feeding neutron-magic ($N = 50$) ^{96}Zr . Some unstable nuclides with relatively long half-lives are able to capture neutrons prior to decay, as illustrated by the thick arrows in Fig. 1. Nuclides such as ^{95}Zr thus become branch points in the *s*-process path, with the branching ratio strongly controlled by activation of the ^{22}Ne reaction. Isotopic compositions resulting from such branches allow identification of grains from parent stars with masses $\geq 3 M_{\odot}$, in which the ^{22}Ne reaction is more strongly activated. Production of ^{96}Zr , and hence the final $^{96}\text{Zr}/^{94}\text{Zr}$ ratio, is strongly affected by the ^{22}Ne neutron source.

The final *s*-process isotopic composition mixed into the envelope by third dredge-up events is modified by the operation of the ^{22}Ne neutron source. Thus, by determining the isotopic compositions of heavy elements in individual presolar grains formed in low-mass AGB stars, we can constrain the impact of the ^{22}Ne neutron source as well as the magnitude of the major ^{13}C neutron source.

A comprehensive description of the postprocessing model of the *s*-process developed by the Torino group is given by Gallino et al. (1998a). Input parameters are obtained from the results of stellar evolution models based on the Frascati Raphson Newton Evolutionary Code (FRANEC) (Straniero et al. 1997). They include the envelope mass, the dredged-up mass, the temperature, and the density at the base of the convective thermal pulse as functions of time. Parameters for the reaction network include nuclear physics data, such as measured or theoretically derived neutron capture cross sections for more than 400 nuclides. Neutron capture occurs on light elements and Fe, as well as on *s*-process elements synthesized in the previous thermal pulse-interpulse cycle.

In the models, the composition of the envelope is calculated as it changes through the sequence of thermal pulses with third dredge-up events. However, for the formation of SiC grains, only the later pulses during which carbon is more abundant in the envelope than oxygen are relevant for two reasons: 1) SiC can form only when the envelope is carbon-rich because, if there is less carbon than oxygen, the formation of CO, a more stable molecule than SiC, locks up all of the carbon, and 2) about one-half of the mass loss occurs during the period of thermal pulsing with the third dredge-up events and the other one-half occurs after the last pulse when the envelope composition is fixed.

A free parameter for these calculations is the amount of ^{13}C in the He-intershell. That value determines the magnitude of the neutron flux and therefore the resulting isotopic compositions of the newly synthesized *s*-process elements. The postprocessing network, coupled with stellar evolution models that consistently produce third dredge-up events, uses parameterization of the ^{13}C pocket efficiencies to generate the full range of neutron exposures from zero to the maximum exposure possible in AGB stars (Lugaro et al. 2003a). The *s*-process models yield results in excellent agreement with astronomical observations of elemental compositions of AGB stars (Busso et al. 2001).

The physical mechanism responsible for mixing protons into the He-intershell has been the subject of much speculation. As stated by Herwig (2005), this mechanism is most likely fundamental to the dynamics of other types of stars as well. Describing this process could be a large step forward in the understanding of stellar dynamics in general, not just in AGB stars. Theories have been reviewed by Lattanzio and Lugaro (2005). They are: 1) semiconvection, in which, after a thermal pulse, a region at the base of the convective envelope becomes semiconvective (i.e., a zone of partial mixing) due to a change in opacity at the base of the envelope (Iben and Renzini 1982); 2) convective overshoot at

the border of any convective/radiative zone, in which a partially mixed zone develops at the base of the envelope. In the models, this is accomplished by the introduction of an exponential decay of the convective velocity based on dynamical simulations (Freytag et al. 1996; Herwig et al. 1997); 3) gravity waves forming at the bottom of the convective envelope due to the buoyancy of displaced parcels at this boundary (Denissenkov and Tout 2003); 4) rotation, in which a partially mixed zone develops between the envelope and core due to differential rotation (Herwig et al. 2003; Siess et al. 2004); and 5) induced overshoot at the base of the convective envelope to account for the thermodynamical instability induced by the discontinuity of the chemical composition between the H-rich envelope and the inner He-rich and C-rich radiative zone (Straniero et al. 2006).

Current models leave a proton profile at the end of a third dredge-up, leading to an additional ^{14}N pocket above the ^{13}C pocket, when the diffused protons reach a higher local concentration so that proton capture on ^{13}C begins to create ^{14}N . Thus the range of neutron exposures in AGB stars is naturally limited (Lugaro 2005).

METHODS

Samples

The objective was to measure the isotopic compositions of multiple heavy elements in a significant number of presolar SiC grains. This required a large number of grains of sufficient size for multi-element analysis. We used the SiC-rich KJH fraction separated from the Murchison CM chondrite by Amari et al. (1994), which contains grains with diameters of 3.4–5.9 μm . The substrate for the grain mount was a 250 μm thick HNO_3 -washed gold foil with an imprint of a $200 \times 200 \mu\text{m}$ grid, which was attached to an SEM post. The grains were suspended in a mixture of isopropanol, water, and HCl, and deposited by pipette onto the foil. When the liquid had evaporated, they were pressed into the foil with a polished sapphire disk.

Secondary electron, backscattered electron, and energy dispersive X-ray (EDX) images of the mount were collected at low magnification using a JEOL JSM-5800LV SEM equipped with an Oxford/Link ISIS-300 X-ray microanalysis system. Si and C EDX maps were used to identify SiC grains. Nearly all of the other grains were determined to be hibonite or corundum on the basis of EDX spectra. Approximately 300 SiC grains were identified, but only about one-half were suitable for analysis because many were too close together (less than $\sim 5 \mu\text{m}$) or too close to hibonite or corundum grains to allow reliable individual grain analysis.

After identification of SiC grains, the mount was re-examined at higher magnification in the SEM to select large grains ($>3 \mu\text{m}$) for RIMS analysis.

Isotopic Analysis of Mo, Zr, and Ba

RIMS on the CHARISMA instrument at Argonne National Laboratory was used to measure heavy element isotopic compositions. A description of the instrument and of its application to presolar grain isotopic analysis is given by Savina et al. (2003b). Briefly, a portion of the grain was ablated with a pulsed laser (spot size $\sim 1 \mu\text{m}$) and tuned lasers were used selectively to ionize elements of interest. Ions were analyzed by time-of-flight mass spectrometry. This method has high sensitivity and strongly suppresses interference from atoms and molecules with the same mass as the element of interest.

The Mo and Ba resonant ionization schemes used here have been employed successfully in previous studies with CHARISMA (Nicolussi et al. 1998b; Savina et al. 2003b). The Mo ionization scheme was $^7\text{S}_3 \rightarrow ^7\text{P}_4^0$ (313.35 nm) (third harmonic of the Ti:sapphire laser fundamental tuned to 940.050 nm), followed by ionization at 388.337 nm (second harmonic of the Ti:sapphire fundamental tuned to 776.674 nm). Wavelengths in this work are given in vacuum, while those in Nicolussi et al. (1998b) for Mo are given in air. The Ba scheme was $^1\text{S}_0 \rightarrow ^1\text{P}_1$ (307.247 nm) (third harmonic of the Ti:sapphire fundamental tuned to 921.741 nm), followed by ionization at 1064.15 nm (Nd:YAG fundamental).

The Zr scheme was different from that used in prior studies. It was developed for this study and tested to ensure that it yielded reliable results. The scheme was $^3\text{F}_2 \rightarrow ^3\text{D}_2$ (296.172 nm) (third harmonic of the Ti:sapphire fundamental tuned to 888.518 nm), followed by ionization at 442.533 nm (Ti:sapphire fundamental tuned to 757.575 nm mixed with 1064.15 nm from a Nd:YAG laser). Zirconium isotope ratios in a terrestrial standard were measured over a range of Ti:sapphire fundamental wavelengths from 888.508–888.528 nm to ensure that slight drift ($\pm 0.003 \text{ nm}$) in the wavelength would not affect the measured isotope ratios. In addition, a high-precision wavemeter was used to monitor the wavelength throughout the procedure to confirm that no drift occurred.

Standards were terrestrial Mo metal, Zr metal, and BaTiO_3 . They were measured daily before grain measurements. Errors arising from Poisson counting statistics were calculated as in Savina et al. (2003b) and are reported here as 2σ . One hundred five grains were analyzed by RIMS and 61 of them had at least one heavy element measured, in addition to the light elements described below. Fifty-three of the 61 were mainstream and are reported here. Most grains yielded between 1000–3000 ion counts of each element. Data from all mainstream grains that yielded ion counts are reported here.

Isotopic Analysis of C, N, and Si

Isotopic compositions of C, N, and Si were measured on the Cameca NanoSIMS-50 at Washington University, Saint

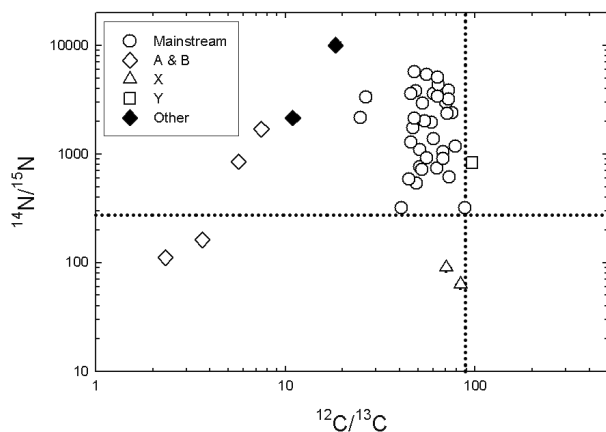


Fig. 2. N versus C isotope ratio plot of KJH SiC grains and classification of grains. Dotted lines at $^{12}\text{C}/^{13}\text{C} = 90$ and $^{14}\text{N}/^{15}\text{N} = 272$ depict terrestrial isotopic ratios for reference.

Louis. Isotopic analyses of C and N are not possible on CHARISMA because C and N have first-excited states above what can be reached with Ti:sapphire lasers. Silicon is problematic because of isobaric interferences from nonresonantly ionized molecules (C_2H_4 and C_2H_5). Because only a small portion of a grain is required for NanoSIMS measurement and because C, N, and sometimes Si measurements are made with a Cs^+ beam, light element measurements were made after all heavy element data had been collected. Cesium has a low ionization potential and is strongly nonresonantly ionized by the CHARISMA lasers. Although RIMS does suppress isobaric interference, the SIMS analysis implants so much ^{133}Cs into the mount and grains that the peak at mass 133 would have a significant tail at masses 134 and possibly 135 (Savina et al. 2003a).

The NanoSIMS standards were synthetic SiC and Si_3N_4 crystals added to the presolar grain mount. The NanoSIMS instrument has a magnetic sector mass spectrometer and five electron multiplier detectors. The Cs^+ source was used and ^{12}C , ^{13}C , ^{28}Si , ^{29}Si , and ^{30}Si negative ions were collected for 105 grains. Subsequently, ^{14}N and ^{15}N were measured by collecting secondary ions at masses 26 ($^{12}\text{C}^{14}\text{N}$) and 27 ($^{12}\text{C}^{15}\text{N}$) along with ^{12}C , ^{13}C and ^{28}Si on 46 grains for which RIMS heavy element measurements had been obtained. Two grains had been totally consumed by RIMS, C and Si analyses and yielded no N data. Standards were measured at regular intervals daily.

RESULTS

The present study is confined to mainstream grains, which were identified by their C, N, and Si isotopic compositions. Molybdenum, Zr, and Ba were used to identify and exclude grains with compositions inconsistent with stellar neutron capture nucleosynthesis, as discussed below. Carbon and N results are presented as isotopic ratios; the others are given in δ -notation.

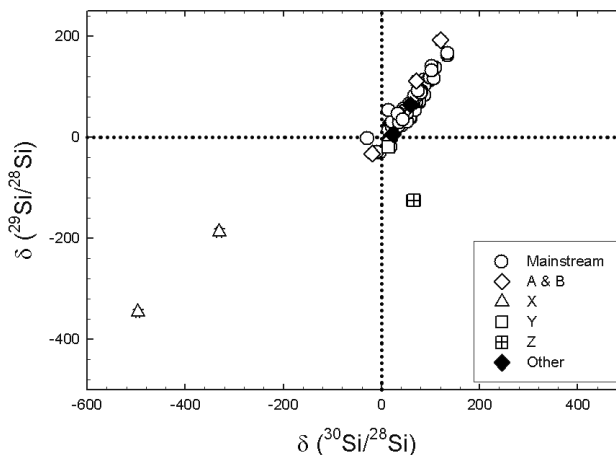


Fig. 3. Si three-isotope plot and classification of grains.

Carbon, Nitrogen, and Silicon

Results for C, N, and Si are shown in Figs. 2 and 3. Four grains meet the criterion for classification as type A + B ($^{12}\text{C}/^{13}\text{C} \leq 10$). Additionally, one grain (with $^{12}\text{C}/^{13}\text{C} \sim 18$) with a heavy element isotopic signature quite different from those of known mainstream grains, and another (with $^{12}\text{C}/^{13}\text{C} \sim 11$) in which no heavy element data were collected, were excluded from the mainstream class. These six grains all had Si isotopic compositions lying along the mainstream correlation line (Fig. 3). Two X grains plot below the mainstream array in Fig. 2. They have excesses of ^{15}N ($^{14}\text{N}/^{15}\text{N} = 90$ and 63) and ^{28}Si (Fig. 3). One has $^{12}\text{C}/^{13}\text{C} = 96$ with a Si isotopic composition slightly to the right of the mainstream line in Fig. 3; it is classified as type Y. The Z grain plotted in Fig. 3 was identified by its depletion of $^{29}\text{Si}/^{28}\text{Si}$ and its excess of $^{30}\text{Si}/^{28}\text{Si}$. Its N isotopic composition was not measured.

All remaining grains have compositions characteristic of the mainstream group: $^{12}\text{C}/^{13}\text{C}$ between 15 and 90, slight enhancements in ^{29}Si and ^{30}Si and falling along a line of slope 1.3 on the Si three-isotope plot. We consider only mainstream grains in the remainder of this study; “alphabet” grains will be discussed elsewhere.

Heavy Elements

Molybdenum isotopic measurements were attempted on 82 grains: 45 yielded detectable Mo signals; of these, 44 were mainstream. Fourteen of the mainstream grains were nearly or entirely consumed during the analysis and it was not possible to detect Zr or Ba in them. Molybdenum results for the 44 mainstream grains are reported in Table 1.

Zirconium analyses were attempted on 52 grains; 41 were successful and of these 33 were mainstream. Twenty-eight also yielded Mo data. In addition, five mainstream grains were analyzed for Zr only (neither Ba nor Mo was attempted). Zirconium results for the 33 mainstream grains are reported in Table 2.

Table 1. Molybdenum data for all mainstream grains ($\pm 2\sigma$). Molybdenum-contaminated grain labels and data are in bold.

| Grain | $\delta^{92}\text{Mo}$ | $\delta^{94}\text{Mo}$ | $\delta^{95}\text{Mo}$ | $\delta^{97}\text{Mo}$ | $\delta^{98}\text{Mo}$ | $\delta^{100}\text{Mo}$ |
|--------------|---------------------------------|---------------------------------|----------------------------------|----------------------------------|----------------------------------|----------------------------------|
| A3-02 | 79 \pm 190 | 26 \pm 208 | 40 \pm 182 | 1 \pm 202 | 81 \pm 171 | 804 \pm 311 |
| A3-05 | -620 \pm 101 | -650 \pm 115 | -374 \pm 137 | -197 \pm 189 | -138 \pm 155 | 276 \pm 261 |
| B2-03 | 36 \pm 189 | 55 \pm 215 | 31 \pm 183 | 148 \pm 224 | 43 \pm 168 | -141 \pm 181 |
| B2-04 | -785 \pm 48 | -770 \pm 60 | -497 \pm 78 | -530 \pm 88 | -235 \pm 94 | -814 \pm 51 |
| B2-06 | 87 \pm 194 | -82 \pm 194 | -120 \pm 161 | -32 \pm 197 | 115 \pm 176 | -244 \pm 165 |
| B3-18 | -704 \pm 44 | -681 \pm 55 | -392 \pm 69 | -333 \pm 86 | -144 \pm 80 | -686 \pm 55 |
| B4-09 | -73 \pm 153 | -139 \pm 167 | 120 \pm 173 | 172 \pm 204 | 336 \pm 188 | 315 \pm 228 |
| B4-14 | -869 \pm 22 | -771 \pm 37 | -448 \pm 52 | -322 \pm 70 | -168 \pm 64 | -803 \pm 35 |
| B4-15 | -770 \pm 80 | -621 \pm 129 | -475 \pm 130 | -305 \pm 186 | 30 \pm 198 | -768 \pm 100 |
| C2-01 | -791 \pm 31 | -817 \pm 34 | -468 \pm 53 | -421 \pm 65 | -227 \pm 62 | -834 \pm 31 |
| C2-03 | -871 \pm 33 | -899 \pm 35 | -595 \pm 63 | -536 \pm 81 | -196 \pm 90 | -927 \pm 28 |
| C2-05 | -749 \pm 34 | -757 \pm 39 | -394 \pm 57 | -271 \pm 75 | -192 \pm 63 | -784 \pm 35 |
| C3-08 | -190 \pm 129 | -186 \pm 147 | -206 \pm 123 | -191 \pm 143 | -158 \pm 116 | -311 \pm 127 |
| C3-09 | -690 \pm 42 | -706 \pm 49 | -353 \pm 67 | -384 \pm 76 | -89 \pm 79 | -618 \pm 57 |
| C3-10 | -918 \pm 31 | -842 \pm 55 | -496 \pm 88 | -393 \pm 117 | -153 \pm 116 | -878 \pm 47 |
| C3-16 | -746 \pm 37 | -671 \pm 51 | -387 \pm 63 | -322 \pm 79 | -167 \pm 72 | -685 \pm 50 |
| C4-01 | -926 \pm 20 | -883 \pm 32 | -529 \pm 58 | -464 \pm 76 | -219 \pm 76 | -913 \pm 27 |
| C4-07 | -861 \pm 29 | -828 \pm 40 | -537 \pm 58 | -427 \pm 79 | -168 \pm 80 | -828 \pm 39 |
| C4-10 | -892 \pm 24 | -829 \pm 38 | -556 \pm 54 | -429 \pm 75 | -193 \pm 75 | -900 \pm 28 |
| C4-20 | -710 \pm 40 | -675 \pm 51 | -403 \pm 62 | -373 \pm 75 | -156 \pm 73 | -706 \pm 48 |
| D2-01 | -879 \pm 33 | -876 \pm 41 | -438 \pm 80 | -480 \pm 90 | -274 \pm 86 | -883 \pm 38 |
| D2-02 | -810 \pm 25 | -798 \pm 31 | -386 \pm 50 | -361 \pm 60 | -277 \pm 51 | -835 \pm 26 |
| D2-03 | -867 \pm 29 | -798 \pm 44 | -578 \pm 55 | -390 \pm 82 | -307 \pm 69 | -896 \pm 29 |
| D2-04 | -652 \pm 89 | -707 \pm 95 | -439 \pm 117 | -343 \pm 152 | -237 \pm 130 | -784 \pm 77 |
| D2-05 | -669 \pm 58 | -718 \pm 62 | -432 \pm 79 | -351 \pm 101 | -197 \pm 91 | -772 \pm 53 |
| D2-09 | -783 \pm 42 | -762 \pm 53 | -427 \pm 74 | -479 \pm 82 | -240 \pm 81 | -767 \pm 50 |
| D2-10 | -805 \pm 42 | -845 \pm 44 | -418 \pm 79 | -453 \pm 89 | -182 \pm 91 | -835 \pm 44 |
| D2-12 | -837 \pm 32 | -779 \pm 45 | -480 \pm 62 | -440 \pm 76 | -276 \pm 70 | -865 \pm 33 |
| D3-05 | -903 \pm 23 | -871 \pm 32 | -571 \pm 54 | -542 \pm 67 | -117 \pm 84 | -900 \pm 29 |
| D3-06 | -857 \pm 31 | -761 \pm 51 | -539 \pm 63 | -373 \pm 91 | -184 \pm 87 | -845 \pm 40 |
| D4-03 | -648 \pm 64 | -653 \pm 75 | -353 \pm 95 | -459 \pm 98 | -121 \pm 110 | -711 \pm 69 |
| F1-02 | -453 \pm 73 | -367 \pm 93 | -217 \pm 91 | -138 \pm 114 | -50 \pm 98 | -336 \pm 99 |
| F2-03 | -476 \pm 77 | -514 \pm 86 | -346 \pm 87 | -259 \pm 111 | -184 \pm 93 | -480 \pm 89 |
| F2-06 | -815 \pm 20 | -766 \pm 28 | -516 \pm 36 | -377 \pm 50 | -250 \pm 45 | -819 \pm 24 |
| F2-09 | -763 \pm 38 | -761 \pm 46 | -447 \pm 63 | -476 \pm 73 | -225 \pm 73 | -733 \pm 50 |
| F2-10 | -804 \pm 31 | -813 \pm 37 | -516 \pm 53 | -406 \pm 73 | -189 \pm 70 | -798 \pm 39 |
| F3-05 | 111 \pm 305 | 236 \pm 373 | -161 \pm 243 | -40 \pm 308 | 48 \pm 265 | -54 \pm 308 |
| G5-02 | -756 \pm 41 | -785 \pm 47 | -466 \pm 63 | -418 \pm 79 | -218 \pm 78 | -882 \pm 33 |
| G5-03 | -901 \pm 19 | -854 \pm 29 | -563 \pm 43 | -526 \pm 54 | -282 \pm 56 | -910 \pm 22 |
| G5-04 | -522 \pm 160 | -530 \pm 187 | -389 \pm 176 | -327 \pm 221 | -280 \pm 184 | -626 \pm 159 |
| H4-03 | -671 \pm 56 | -711 \pm 62 | -482 \pm 70 | -327 \pm 98 | -243 \pm 85 | -895 \pm 35 |
| H4-04 | -823 \pm 30 | -770 \pm 42 | -488 \pm 53 | -438 \pm 67 | -242 \pm 65 | -863 \pm 31 |
| H4-06 | -696 \pm 62 | -693 \pm 75 | -321 \pm 98 | -453 \pm 99 | -144 \pm 108 | — |
| H4-07 | -872 \pm 40 | -808 \pm 60 | -536 \pm 79 | -536 \pm 94 | -377 \pm 90 | -923 \pm 36 |

Barium measurements were attempted on 41 grains; 26 were successful, of which 23 were mainstream. Seventeen of these were analyzed for all three heavy elements; two were analyzed for Mo and Ba only and four were analyzed for Ba only. Barium results for the 23 mainstream grains are reported in Table 3. The isotopes ^{130}Ba and ^{132}Ba are not reported because their abundances were too low.

The results for individual elements, discussed in the next section, are similar to those obtained in previous studies of

Mo (Nicolussi et al. 1998b), Zr (Nicolussi et al. 1997), and Ba (Savina et al. 2003a). Because the goal here was to measure multiple heavy elements in single grains, care was taken not to consume an entire grain during the measurement procedure. This resulted in fewer counts per grain and correspondingly larger errors than measurements in prior studies. The primary difference between our results and those from prior studies—i.e., the distribution of the data on three-isotope plots—is discussed below.

Table 2. Zirconium data for all mainstream grains ($\pm 2\sigma$).

| Grain | $\delta^{90}\text{Zr}$ | $\delta^{91}\text{Zr}$ | $\delta^{92}\text{Zr}$ | $\delta^{96}\text{Zr}$ |
|-------|------------------------|------------------------|------------------------|------------------------|
| A3-01 | -138 ± 102 | -85 ± 139 | 16 ± 143 | -555 ± 172 |
| A3-05 | -75 ± 105 | -152 ± 127 | 24 ± 139 | -545 ± 168 |
| B2-04 | -197 ± 80 | -242 ± 99 | -71 ± 110 | -812 ± 93 |
| B2-06 | -56 ± 94 | -43 ± 121 | 72 ± 126 | -457 ± 162 |
| B4-14 | -70 ± 96 | -139 ± 118 | -35 ± 122 | -856 ± 84 |
| B4-15 | -253 ± 122 | -291 ± 156 | -148 ± 169 | -803 ± 151 |
| C2-04 | -97 ± 124 | -172 ± 149 | -28 ± 160 | -686 ± 166 |
| C3-16 | -239 ± 127 | -256 ± 166 | 90 ± 210 | -643 ± 213 |
| C4-07 | -52 ± 99 | -142 ± 118 | -56 ± 121 | -782 ± 105 |
| C4-10 | -234 ± 104 | -332 ± 126 | -127 ± 145 | -862 ± 106 |
| C4-20 | 75 ± 163 | -11 ± 193 | 165 ± 209 | -142 ± 325 |
| D2-01 | -236 ± 89 | -294 ± 111 | -219 ± 114 | -801 ± 112 |
| D2-02 | -257 ± 78 | -155 ± 113 | -145 ± 109 | -669 ± 131 |
| D2-03 | -361 ± 62 | -423 ± 78 | -251 ± 89 | -701 ± 112 |
| D2-04 | -198 ± 55 | -226 ± 70 | -122 ± 73 | -876 ± 51 |
| D2-09 | -213 ± 88 | -195 ± 116 | -168 ± 114 | -693 ± 134 |
| D2-10 | -226 ± 80 | -330 ± 94 | -236 ± 99 | -563 ± 149 |
| D2-12 | -266 ± 69 | -233 ± 94 | -195 ± 93 | -766 ± 98 |
| D3-06 | -135 ± 120 | -207 ± 147 | -31 ± 162 | -745 ± 151 |
| D4-03 | -103 ± 124 | -176 ± 152 | 102 ± 179 | -82 ± 302 |
| E1-09 | -159 ± 83 | -205 ± 103 | 17 ± 118 | -601 ± 138 |
| F1-02 | -209 ± 94 | -173 ± 128 | -130 ± 127 | -848 ± 97 |
| F2-03 | -191 ± 112 | -134 ± 152 | -68 ± 154 | -740 ± 154 |
| F2-06 | -307 ± 85 | -370 ± 106 | -203 ± 119 | -902 ± 81 |
| F2-09 | -191 ± 95 | -254 ± 116 | -160 ± 121 | -718 ± 136 |
| F3-07 | -110 ± 109 | 18 ± 156 | -15 ± 145 | -540 ± 181 |
| G3-04 | -205 ± 60 | -141 ± 82 | -25 ± 87 | -539 ± 109 |
| G5-02 | -212 ± 91 | -213 ± 119 | -127 ± 123 | -843 ± 96 |
| G5-03 | -204 ± 91 | -227 ± 117 | -167 ± 118 | -776 ± 114 |
| G5-04 | -103 ± 153 | -183 ± 185 | 105 ± 221 | -516 ± 260 |
| H4-03 | -326 ± 66 | -149 ± 105 | -94 ± 105 | -709 ± 109 |
| H4-04 | -291 ± 60 | -228 ± 84 | -151 ± 86 | -748 ± 90 |
| H4-06 | -143 ± 104 | -285 ± 118 | -27 ± 141 | -576 ± 176 |

DISCUSSION

Identification of Isotopically Unusual Grains

Figures 4 and 5 are multi-element/multi-isotope plots of mainstream SiC grains. Model predictions for AGB stars of 1.5 and 3 M_{\odot} are also plotted. The model began with solar elemental and isotopic composition and metallicity and evolved along the asymptotic giant branch with a range of ^{13}C pocket efficiencies. The standard case (ST) is the ^{13}C pocket efficiency required to produce the solar s -process elemental distribution in models of AGB stars of one-half solar metallicity (Arlandini et al. 1999). The minimum ^{13}C pocket efficiency is D12, which is the standard case divided by 12 and corresponds to the near-absence of the ^{13}C pocket. The maximum ^{13}C pocket efficiency is U2, which is the standard case multiplied by 2 and corresponds to the natural limit set by the activation of the reaction $^{13}\text{C}(p,\gamma)^{14}\text{N}$ when the local concentration of protons diffused from the envelope becomes high enough. Each model point in the plots corresponds to the isotopic composition of the stellar envelope after a thermal

Table 3. Barium data for all mainstream grains ($\pm 2\sigma$).

| Barium-contaminated grain labels and data are in bold. | | | | |
|--|----------------------------------|----------------------------------|----------------------------------|----------------------------------|
| Grain | $\delta^{134}\text{Ba}$ | $\delta^{135}\text{Ba}$ | $\delta^{137}\text{Ba}$ | $\delta^{138}\text{Ba}$ |
| B2-04 | 37 ± 392 | -669 ± 130 | -266 ± 188 | -77 ± 180 |
| B2-06 | 517 ± 604 | -47 ± 318 | 48 ± 300 | -68 ± 219 |
| B4-01 | -170 ± 246 | -848 ± 56 | -568 ± 91 | -352 ± 96 |
| B4-11 | -34 ± 240 | -210 ± 143 | -200 ± 129 | -327 ± 88 |
| C3-01 | 15 ± 200 | -596 ± 76 | -379 ± 85 | -282 ± 73 |
| C3-09 | -145 ± 254 | -568 ± 112 | -298 ± 132 | -329 ± 97 |
| C3-15 | 15 ± 200 | -596 ± 76 | -379 ± 85 | -282 ± 73 |
| C3-16 | 497 ± 438 | -651 ± 119 | -387 ± 145 | -249 ± 130 |
| C4-20 | 445 ± 497 | -536 ± 165 | -416 ± 162 | -222 ± 157 |
| D2-02 | -477 ± 426 | -359 ± 325 | -399 ± 263 | -232 ± 246 |
| D2-04 | 591 ± 586 | -651 ± 153 | -419 ± 179 | -287 ± 160 |
| D2-10 | 46 ± 396 | -576 ± 153 | -418 ± 159 | -205 ± 157 |
| D2-12 | -125 ± 295 | -729 ± 96 | -391 ± 136 | -281 ± 119 |
| D3-06 | 185 ± 338 | -720 ± 93 | -526 ± 108 | -415 ± 93 |
| D4-03 | -264 ± 356 | -624 ± 158 | -90 ± 248 | -79 ± 200 |
| F2-09 | 110 ± 448 | -303 ± 231 | -279 ± 203 | -172 ± 177 |
| G5-02 | 258 ± 438 | -765 ± 105 | -301 ± 179 | -293 ± 138 |
| G5-03 | 786 ± 762 | -418 ± 255 | 94 ± 351 | -19 ± 260 |
| G5-04 | 107 ± 354 | -642 ± 118 | -328 ± 152 | -305 ± 119 |
| H4-03 | 148 ± 359 | -729 ± 99 | -489 ± 123 | -326 ± 115 |
| H4-04 | 425 ± 485 | -266 ± 221 | -13 ± 238 | -92 ± 178 |
| H4-06 | -89 ± 319 | -201 ± 205 | -141 ± 187 | -141 ± 148 |
| H4-07 | -120 ± 254 | -178 ± 169 | -123 ± 154 | -125 ± 122 |

pulse in which the envelope is carbon-rich. For example, the filled squares correspond to the model of a 3 M_{\odot} AGB star with a ^{13}C pocket efficiency 1.5 times less than that of the ST case (D1.5).

Figure 4 is a plot of ($^{96}\text{Zr}/^{94}\text{Zr}$) versus ($^{92}\text{Mo}/^{96}\text{Mo}$) for the 28 grains for which both Mo and Zr were measured. Twenty-one grains lie within 2σ of model predictions, while seven (B2-04, B2-06, D2-04, F1-02, F2-03, F2-06, G5-02) have compositions differing by more than 2σ . Error ellipses for these seven grains are shown and these grains are indicated in bold in Table 1.

Figure 5 is a plot of ($^{96}\text{Zr}/^{94}\text{Zr}$) versus ($^{135}\text{Ba}/^{136}\text{Ba}$) for the 17 mainstream grains for which both Ba and Zr were measured. Five grains (D2-04, F2-09, G5-03, H4-04, H4-07) have compositions more than 2σ from the predictions and are shown with error ellipses. These grains are indicated in bold in Table 3. Additionally, two grains with large errors (B2-06, H4-06) are almost exactly 2σ from model predictions.

Figures 4 and 5 depict grains with compositions inconsistent with model predictions—or any neutron capture process. The neutron exposure affecting the $^{92}\text{Mo}/^{96}\text{Mo}$ ratio must also affect the $^{96}\text{Zr}/^{94}\text{Zr}$ and $^{135}\text{Ba}/^{136}\text{Ba}$ ratios. The Zr-Nb-Mo section of the chart of the nuclides is in Fig. 1. The production of ^{96}Zr is strongly affected by activation of the ^{22}Ne neutron source; only at high neutron flux is ^{96}Zr produced via neutron capture on short-lived ^{95}Zr . This is evident as the 3 M_{\odot} model predictions curve up and away from a slope-one line connecting the origin and $(-1000, -1000\%)$ on Figs. 4 and 5. For any ^{13}C pocket efficiency,

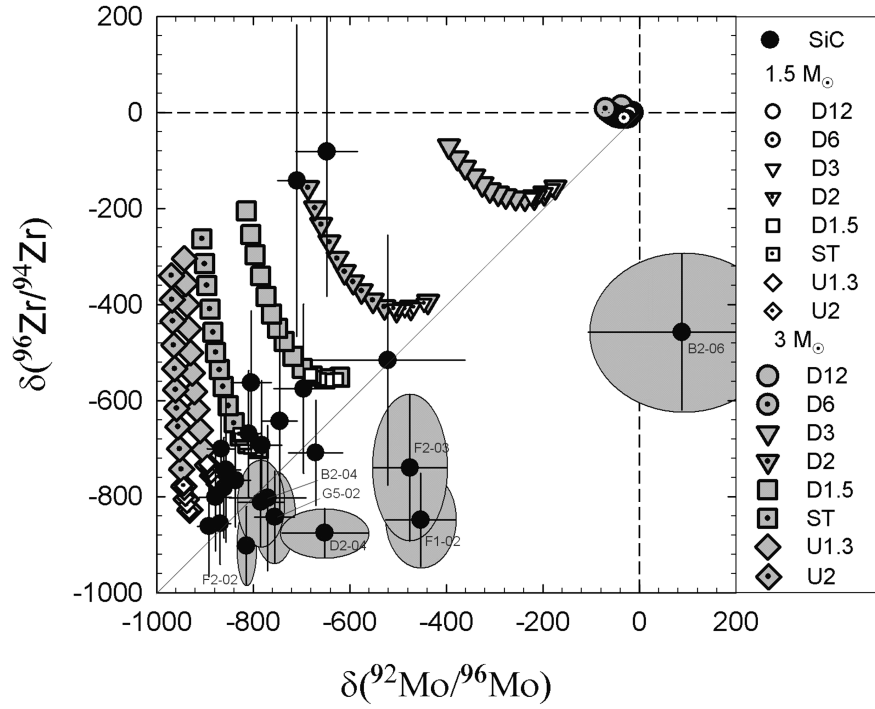


Fig. 4. Plot of $\delta(^{96}\text{Zr}/^{94}\text{Zr})$ versus $\delta(^{92}\text{Mo}/^{96}\text{Mo})$ used for the identification of Mo-contaminated grains. Solid circles are SiC grain data from this study; error bars are 2σ . Model predictions for stars of solar metallicity and $1.5 M_{\odot}$ are plotted as open symbols and of $3 M_{\odot}$ as gray-filled symbols. The model predictions are shown for an assumed range of neutron exposures from D12 (minimum) to U2 (maximum). The grains for which error ellipses are shown are $>2\sigma$ away from model predictions.

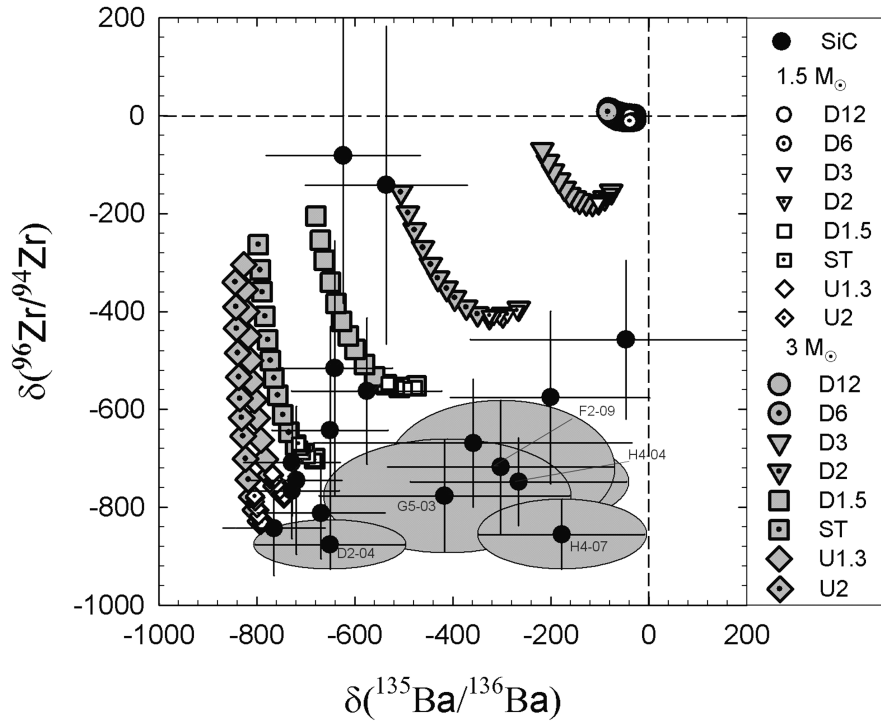


Fig. 5. Plot of $\delta(^{96}\text{Zr}/^{94}\text{Zr})$ versus $\delta(^{135}\text{Ba}/^{136}\text{Ba})$ used for the identification of Ba-contaminated grains. Solid circles are SiC grain data from this study; error bars are 2σ . Model predictions for stars of solar metallicity and $1.5 M_{\odot}$ are plotted as open symbols and of $3 M_{\odot}$ as gray-filled symbols. The model predictions are shown for an assumed range of neutron exposures from D12 (minimum) to U2 (maximum). The grains for which error ellipses are shown plot $>2\sigma$ away from model predictions.

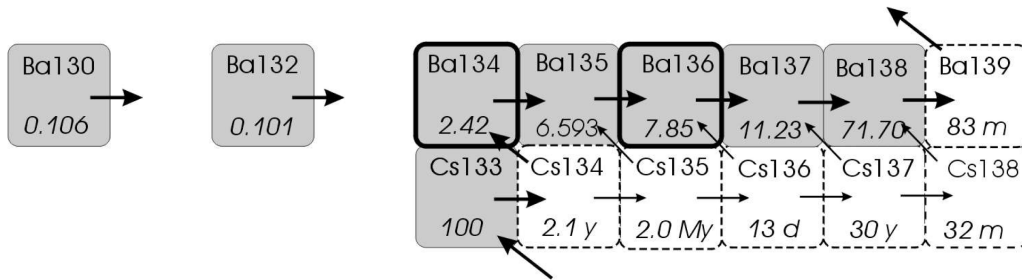


Fig. 6. The Cs to Ba section of the chart of the nuclides. The main path of the *s*-process is shown with thick arrows. Alternative paths are indicated with thin arrows. Stable nuclides are dark gray and unstable nuclides are white. Abundances in percent are shown for the stable and half-lives for the unstable nuclides.

the envelope of the 3 M_{\odot} star has higher $^{96}\text{Zr}/^{94}\text{Zr}$ ratios than does that of the 1.5 M_{\odot} star, reflecting the increasing activation of the ^{22}Ne source with greater stellar mass. Figure 1 shows that ^{92}Mo is bypassed by the *s*-process. There is no way to produce ^{92}Mo via neutron capture, and the $^{92}\text{Mo}/^{96}\text{Mo}$ ratio can decrease only due to neutron exposure as *p*-only ^{92}Mo is consumed. This means that while compositions above the model predictions in Fig. 4 are possible given an appropriate neutron flux, compositions below the slope-one line cannot be produced under any *s*-process conditions. Thus the isotopic compositions of the seven grains in this region that lie greater than 2σ from the model predictions cannot be produced by the *s*-process, independent of the choice of models, provided one begins with an initially solar-like composition.

These seven grains also deviate from model predictions in plots of $\delta(^{96}\text{Zr}/^{94}\text{Zr})$ versus $\delta(^{94}\text{Mo}/^{96}\text{Mo})$ and $\delta(^{100}\text{Mo}/^{96}\text{Mo})$ (not shown). (Molybdenum-94 is *p*-only and ^{100}Mo is *r*-only.) Smaller deviations and larger uncertainties coupled with a large spread in predictions preclude a similar analysis for ^{95}Mo , ^{97}Mo , and ^{98}Mo . While the initial compositions of the stellar progenitors are unknown, they would have to be strongly enhanced in both *p*- and *r*-process Mo to produce the observed ratios. If this were the case, ^{96}Zr (predominantly *r*-process) would also be expected to be enhanced, driving the compositions upward in Fig. 4 and making it unlikely to see grains below the model predictions. We are unable to assess this effect quantitatively, but it appears unlikely that stellar progenitors with strongly nonsolar initial compositions were responsible for the compositions of these grains.

Interpretation of Fig. 5 is similar to that of Fig. 4. However, the case here is not so straightforward. Barium-135 is predominantly *r*-process, but is weakly produced by the *s*-process at low neutron flux when ^{134}Cs decays before capturing a neutron, as shown in Fig. 6. Thus the slope-one line does not serve as an absolute dividing line as in the case of ^{92}Mo , and deviations (i.e., points below the line) are apparent for some models with ^{13}C pocket efficiencies below the ST case in Fig. 5. Thus classification of the five grains as deviant depends upon model inputs. Neutron capture cross

sections for Ba are well known, with uncertainties on the order of only 2%, and adjusting them within their uncertainties has a negligible effect on model predictions. In contrast, the cross sections for unstable Cs isotopes are largely unknown (Bao et al. 2000; Lugaro et al. 2003a). The cross section for ^{135}Cs has been measured to an accuracy of 8%, but those for ^{134}Cs , ^{136}Cs , and ^{137}Cs are only theoretical estimates (Bao et al. 2000). As for beta-decay rates, the temperature dependency of the ^{134}Cs rate has been studied by Takahashi and Yokoi (1987) but is uncertain. Cesium-135 likely has a long enough half-life at the temperature of the ^{13}C pocket that it can be assumed to act as if it were stable. We have not calculated model predictions in which the unstable Cs isotope cross sections and decay rates are varied within their estimated uncertainties and thus cannot quantitatively assess the effect.

Marhas et al. (this issue) have also measured Ba isotopic compositions in presolar SiC grains and have shown by other methods that some grains are contaminated with solar system Ba. They find that uncontaminated grains have $\delta(^{135}\text{Ba}/^{136}\text{Ba})$ lower than about -400% . Of the five grains classified as deviant here, only one, D2-04, has $\delta(^{135}\text{Ba}/^{136}\text{Ba})$ significantly less than -400% , with a value of $\delta(^{135}\text{Ba}/^{136}\text{Ba}) = -651\%$. Its 2σ error ellipse is extremely close to the model prediction (Fig. 5); however, it was also classified as deviant on the basis of its Mo isotopic composition. It is likely to be only mildly contaminated with Ba. Figure 4 also shows three grains classified as uncontaminated but with $\delta(^{135}\text{Ba}/^{136}\text{Ba})$ greater than -400% . All three have large error bars just barely touching the model predictions. Under our definition these three grains are uncontaminated; however, more precise measurements might have resulted in a different classification.

It is possible that the deviant grains in Fig. 5 had *r*-process enhanced (i.e., ^{135}Ba -rich) progenitor stars. Of the nine for which Mo, Zr, and Ba were all measured, only D2-04 is anomalous with respect to both Mo and Ba. It is difficult to imagine initial stellar compositions that could account for this since, if the initial composition was *r*-enhanced, we would expect that to be evident from the abundances of all *r*-process nuclides, which is not the case.

Grain Contamination

The simplest explanation for the compositions of deviant grains is selective elemental contamination with solar system material. Grains have a long history between the point at which they condense around stars and the moment they are analyzed in the laboratory. They have come into contact with materials of terrestrial (solar) composition in the host meteorite, during extraction from the meteorite, and during preparation for analysis. We consider each of these possibilities in turn.

Contamination with Mo and/or Ba (not Zr) might result from differences in the solubilities of these elements in water. The concentrations of Mo ($\sim 10^{-7}$ mol kg $^{-1}$ as MoO_4^{2-}) and Ba ($\sim 10^{-7}$ mol kg $^{-1}$ as Ba^{2+}) relative to Zr ($\sim 10^{-10}$ mol kg $^{-1}$ as $\text{Zr}(\text{OH})_5^-$ and $\text{Zr}(\text{OH})_4^0$) in sea water indicate that Mo and Ba are considerably more soluble than Zr (Bruland and Lohan 2003). Contamination may have occurred during aqueous activity on the meteorite parent body as Mo and Ba, but not Zr, were leached from minerals and deposited on or within the SiC grains. Finding that not all grains are contaminated is consistent with this since aqueous alteration could have occurred locally on a small scale (<1 cm) on the parent body. Additional support comes from the finding that Ba isotopic compositions of presolar grains from Indarch (Jennings et al. 2002) differ from those from Murchison (Savina et al. 2003a). The Indarch grains have a more typically *s*-process component (i.e., plot farther from the origin) than do those from Murchison (Lugaro et al. 2003a). This can be explained if the Indarch parent body underwent no aqueous alteration, whereas the Murchison parent body did, and thus the former contains presolar SiC grains that are generally less contaminated by asteroidal aqueous alteration. The mineralogies of these meteorites (Murchison as described by Fuchs et al. [1973]; Indarch by Keil [1968]) indicate that Murchison underwent aqueous alteration whereas Indarch did not.

Another potential source of contamination is the grain separation procedure. It has been shown that separation procedures may have effects on grain composition (Bernatowicz et al. 2003; Henkel et al. 2006). In the latter study, SiC grains gently separated from a meteorite through freeze-thaw methods without chemical dissolution were found to contain a Mg- and Ca-bearing outer layer not present on grains separated by the harsh chemical dissolution method used on our sample. Gently separated grains also behaved differently during sputtering, with some becoming uneven and pitted, while all of the acid-extracted grains remained smooth throughout sputtering. Thus the separation procedure changes the grain surface and potentially its interior, and may introduce or remove contaminants.

Grains from Murchison and Indarch underwent identical separation procedures except that Murchison separates were treated with concentrated H_2SO_4 to dissolve oxides, whereas

Indarch separates were not. It is possible that this introduced contamination or made the grains more susceptible to it. Noble-metal nuggets are often present in grain separates since they are not dissolved in the separation procedure (Merchel et al. 2003; Kashiv 2004). Molybdenum is commonly associated with noble elements—one SiC grain with high Ru and Mo contents, measured by synchrotron X-ray fluorescence, was found to contain elevated concentrations of Ir and Os (Kashiv 2004)—suggesting that some Mo of solar composition may survive the meteorite dissolution procedure and come into contact with SiC grains. During the RIMS analysis, deposits containing Mo of terrestrial isotopic composition were found in one region of the mount. When areas of high Mo background were observed, it was discovered that small particles containing Mo were deposited in ring-like patterns—apparently from evaporation of a liquid droplet. This indicates that some material much finer than the SiC grains was suspended in the liquid and deposited along with the grains. Grains in this area of Mo contamination were not analyzed in this study. The great majority of the mount was free from any detectable Mo background. Similarly, Marhas et al. (this issue) found Ba contamination on regions of a mount through ion imaging in the nanoSIMS and chose to exclude grains from those regions in their analyses.

Most deviant grains appear to have been contaminated with either Mo or Ba of terrestrial isotopic composition; only one was contaminated with both. Since the analysis sequence was Mo-Zr-Ba, this could reflect a depth dependence of the contamination revealed during the laser ablation process, which would in turn indicate that only grain surfaces are contaminated. The first step of the RIMS analysis was done with the laser tuned to Mo and sampled the top surface of the grain plus a portion of its interior. During the second stage, with the lasers tuned to Zr, interiors were sampled because the tops of the grains had been removed. The third stage (Ba) sampled the interior and in some cases a portion of the bottom surface. Secondary electron images made after RIMS analysis showed that many grains had been almost completely consumed. If contamination is carried primarily on the surface, this sequence could account for the observation that most deviant grains were apparently contaminated in only one element. The fact that not all grains show contamination may be explained if some have different textures from others—for example, if some contain fissures while others do not. The former may acquire and retain contamination whereas more monolithic grains might not.

We next consider findings for Mo, Zr, and Ba in light of previous work and AGB model predictions.

Molybdenum

Figure 7 is a Mo three-isotope plot for mainstream grains. There are three types of grains: 7 contaminated, 21 uncontaminated, and 16 with unknown status—because only

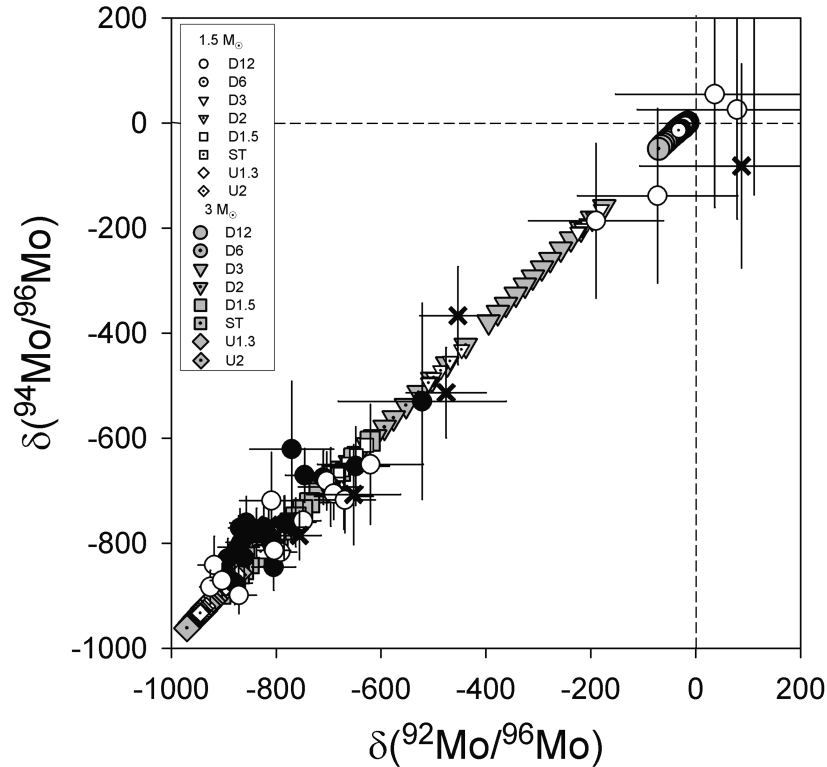


Fig. 7. Plot of $\delta(^{94}\text{Mo}/^{96}\text{Mo})$ versus $\delta(^{92}\text{Mo}/^{96}\text{Mo})$ used to constrain ^{13}C pocket efficiencies showing data for all grains on which Mo was measured along with model predictions. Solid circles are SiC grains from this study classified as uncontaminated; crosses are SiC grains classified as contaminated; open symbols are SiC grains from this study in which Mo but not Zr was measured and therefore whose contamination status cannot be determined. Error bars are 2σ .

Mo was measured. These 16 grains are those in which no Zr was detected. This may be a result of low concentrations of Mo and/or Zr, making it impossible to measure more than one heavy element (i.e., the Mo analysis consumed nearly all of the grain). Alternatively, it may be that some contained little or no stellar Mo or Zr and that the Mo found is all, or nearly all, contamination of terrestrial origin. However, some grains did have Mo *s*-process signatures and apparently lacked only Zr.

Together these data are comparable to those from a prior study in which only Mo was measured (Nicolussi et al. 1998b). Most grains in Fig. 7 cluster at the lower left with $\delta(^{92}\text{Mo}/^{96}\text{Mo})$, $\delta(^{94}\text{Mo}/^{96}\text{Mo})$, and $\delta(^{100}\text{Mo}/^{96}\text{Mo})$ values below -600% , while the others are in a line extending to the origin. In the prior study, 70% of the analyzed grains (16 of 23) had $\delta(^{92,94,100}\text{Mo}/^{96}\text{Mo}) < -600\%$, while in this work 80% do (35 of 44). However, 20 of 21 uncontaminated grains plot below -600% , while only four of seven contaminated ones do. Of the 16 grains of unknown status, eleven (70%) have $\delta(^{92,94,100}\text{Mo}/^{96}\text{Mo}) < -600\%$. It appears that nearly all grains with $\delta(^{92,94,100}\text{Mo}/^{96}\text{Mo}) > -600\%$ are contaminated with material of terrestrial composition.

In the following, we consider only mainstream grains that were categorized as uncontaminated on the basis of Figs. 4 and 5.

Figure 8 contains all Mo three-isotope plots, comparing model predictions with data from uncontaminated grains. Whereas previous results required the entire range of neutron exposures—generated by ^{13}C pocket efficiencies ranging from D12 to U2—we find that a limited range of ^{13}C pocket efficiencies is sufficient for uncontaminated grains. All have isotopic compositions within 2σ of predictions for ^{13}C pocket efficiencies in the range from D1.5 to U1.3 in Fig. 8. The data and models agree well for $(^{94}\text{Mo}/^{96}\text{Mo})$ versus $(^{92}\text{Mo}/^{96}\text{Mo})$. (Both ^{92}Mo and ^{94}Mo are *p*-process isotopes.) The models predict slightly lower $^{94}\text{Mo}/^{96}\text{Mo}$ and $^{92}\text{Mo}/^{96}\text{Mo}$ ratios than are observed, which is consistent with previous results (see Figs. 8 and 9 of Lugaro et al. 2003a). It has been suggested that this arises from slightly incorrect neutron capture cross sections in the models.

In the plot of $\delta(^{95}\text{Mo}/^{96}\text{Mo})$ versus $\delta(^{92}\text{Mo}/^{96}\text{Mo})$ (Fig. 8) observations fall below model predictions. This is consistent with the results of Nicolussi et al. (1998b) and was discussed by Lugaro et al. (2003a), who suggested that it could be explained if the cross section of ^{95}Mo were increased by 30%. This is within the realm of possibility given the scatter in measurements of the neutron capture cross section (Bao et al. 2000).

Experimental data here are also below predictions in the $\delta(^{97}\text{Mo}/^{96}\text{Mo})$ versus $\delta(^{92}\text{Mo}/^{96}\text{Mo})$ and $\delta(^{98}\text{Mo}/^{96}\text{Mo})$ versus

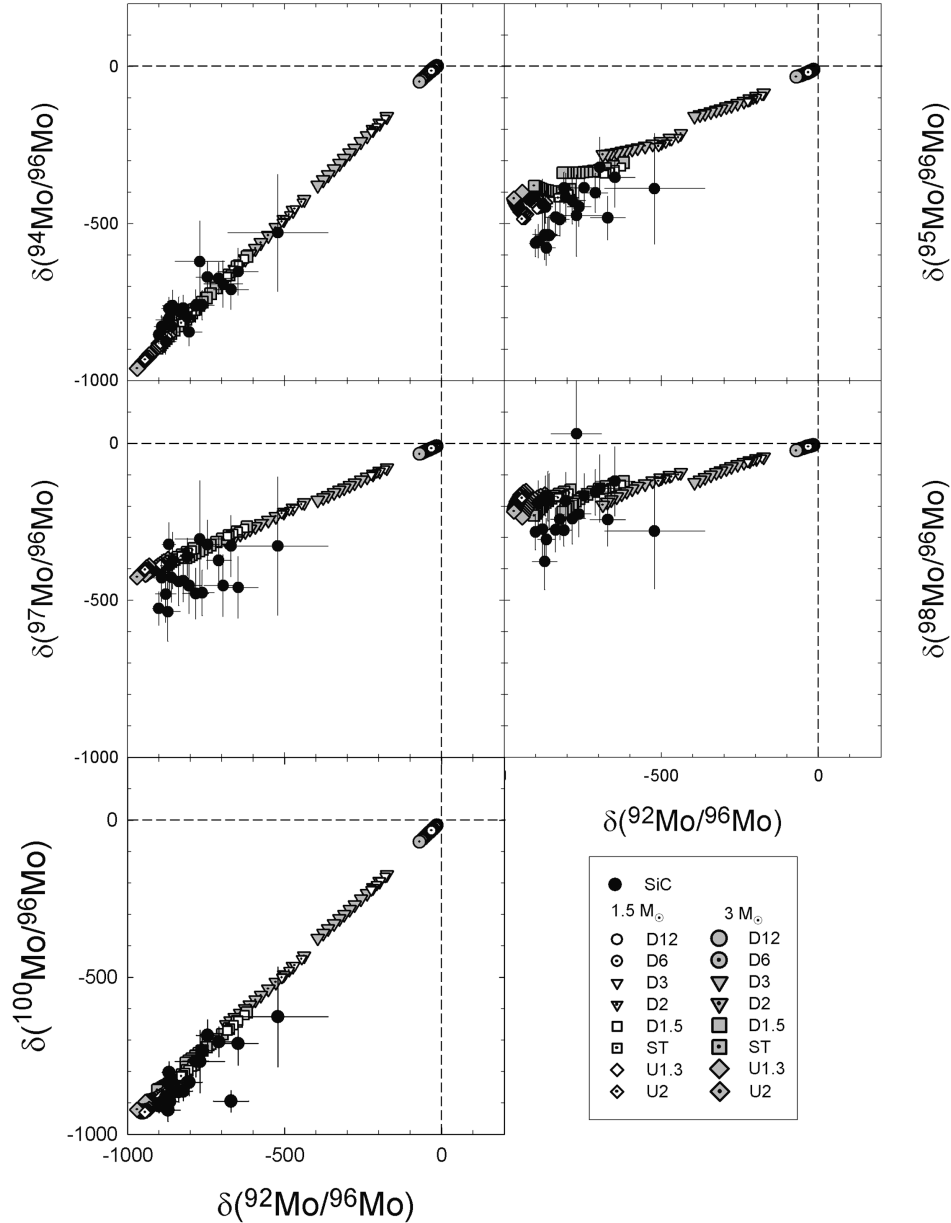


Fig. 8. Three-isotope plots for Mo showing all non-contaminated grain data and model predictions. Solid circles are SiC grains from this study; error bars are 2σ .

$\delta(^{92}\text{Mo}/^{96}\text{Mo})$ plots. This was not seen in prior studies (Lugaro et al. 2003a; Nicolussi et al. 1998b), and there is no obvious explanation for the discrepancy between the two data sets. Model predictions here are sensitive to the ^{97}Mo and ^{98}Mo cross sections, and to the branch point at ^{95}Zr , since neutron capture on ^{95}Zr leads to ^{96}Zr and then to ^{97}Zr , which decays to ^{97}Mo , reducing the amount of ^{96}Mo produced relative to ^{97}Mo and ^{98}Mo . The recommended neutron capture cross sections of Mo and Zr are based on relatively old measurements with stated uncertainties of 10%. We urge that more accurate and precise measurements be made using the more advanced techniques available.

The final panel of Fig. 8 shows $(^{100}\text{Mo}/^{96}\text{Mo})$ versus $(^{92}\text{Mo}/^{96}\text{Mo})$. Depletion of r -only ^{100}Mo is linearly correlated with that of p -only ^{92}Mo since neither isotope is produced by the s -process. Model predictions agree well with the data except for one grain (H4-03) that falls significantly below the line. Contamination seems unlikely since only one isotope is affected. Isobaric interference at mass 92 (or a true enhancement in ^{92}Mo) is also not possible since this grain would then appear deviant on the $\delta(^{94}\text{Mo}/^{96}\text{Mo})$ versus $\delta(^{92}\text{Mo}/^{96}\text{Mo})$ plot, which is not the case. Thus, this grain appears to be significantly depleted in ^{100}Mo relative to ^{92}Mo . This may be a reflection of the initial composition of the

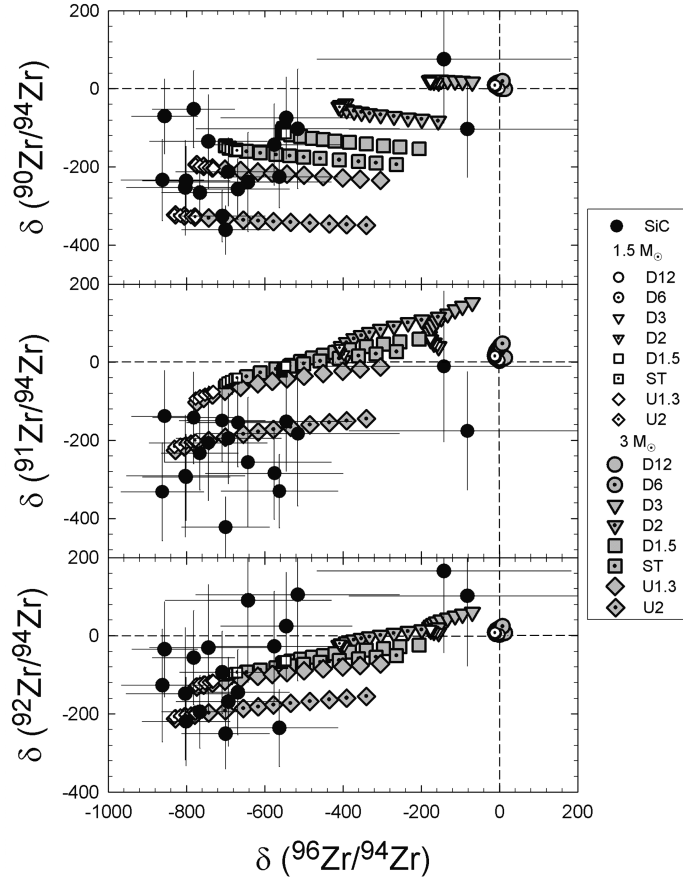


Fig. 9. Three-isotope plots for Zr showing all non-contaminated grain data and model predictions.

parent star, which may have been depleted in *r*-process isotopes. In fact, this grain is also somewhat depleted in the partially *r*-process isotope ^{95}Mo compared to both its neighbors and the models, although here the spread in the data and predictions makes interpretation difficult. Its depletion in the other mainly *r*-process isotopes studied here, ^{96}Zr and ^{135}Ba , is large but not anomalously so (Tables 2 and 3).

Zirconium

Figure 9 has three-isotope plots and model predictions for Zr. Again, there is generally good agreement between data from uncontaminated grains and model predictions, though there is curvature and a large spread in the model predictions resulting from branch points at ^{95}Zr and ^{89}Sr and from the large dependence of the plotted ratios on the ^{13}C pocket efficiency. Several grains are more depleted in ^{91}Zr than predicted. However, a plot of $\delta(^{90}\text{Zr}/^{94}\text{Zr})$ versus $\delta(^{91}\text{Zr}/^{94}\text{Zr})$ does not show a corresponding depletion in ^{90}Zr that would result from interference at mass 94.

All Zr plots show two grains (C4-20 and D4-03) near the origin but with large uncertainties. They are not, however, unusual in their Mo or Ba compositions (Tables 1 and 3; Figs. 8 and 10). They are also outliers on multi-

element plots (Figs. 4 and 5) where they are the only grains requiring $3 M_{\odot}$ models to explain their compositions. Although it is impossible to rule out Zr contamination, that is not a likely cause. First, the compositions can be explained by activation of the ^{22}Ne neutron source, which results in increased production of ^{96}Zr . For Mo and Ba, grains identified as contaminated did not have compositions consistent with the *s*-process. While the multi-element plots require ^{13}C pocket efficiencies of the D2 or D1.5 cases for these two grains, the D3 case or smaller might be indicated on the Zr three-isotope plots. The Zr plots also differ from the Mo and Ba ones in that several grains have ^{96}Zr depletions greater than predicted by the model. This has been seen in previous work and several factors may be involved, including uncertainty in the ^{95}Zr cross section as noted above, or uncertainty in the ^{22}Ne reaction rate, which strongly affects the branch point at ^{95}Zr (Lugaro et al. 2003a).

Barium

Figure 10 presents three-isotope plots for Ba and model predictions. The non-linearity of predictions is caused primarily by an increased neutron flux resulting in deviations

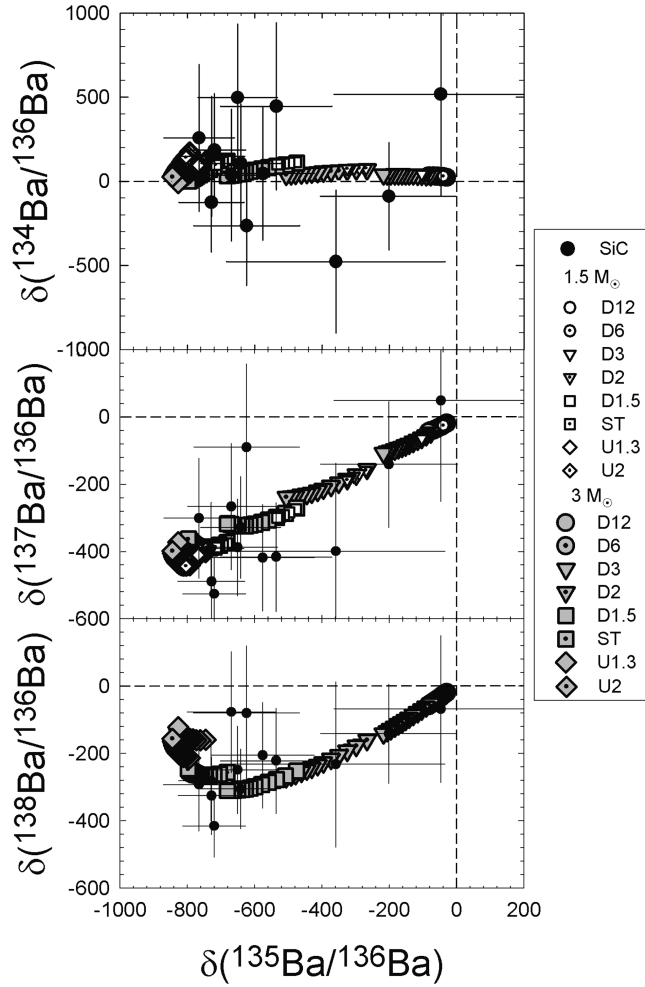


Fig. 10. Three-isotope plots for Ba showing all non-contaminated grain data and model predictions.

from the main s -process path. Neutron capture on ^{133}Cs creates ^{134}Cs ($t_{1/2} = 2.1$ yr) which β^- decays into s -only ^{134}Ba . At higher neutron densities, $^{135}, ^{136}, ^{137}, ^{138}\text{Cs}$ may be created and β^- decay to the corresponding isotopes of Ba (^{135}Cs is stable on s -process time scales) (Fig. 6). In the $\delta(^{134}\text{Ba}/^{136}\text{Ba})$ versus $\delta(^{135}\text{Ba}/^{136}\text{Ba})$ plot in Fig. 10, predicted values are non-linear for $\delta(^{134}\text{Ba}/^{136}\text{Ba})$ because, at the low neutron flux during the early AGB phase, ^{134}Ba is produced by β^- decay of ^{134}Cs , while at the higher flux during the late AGB phase, neutron capture competes with β^- decay, at which point both ^{134}Ba and ^{135}Ba are bypassed. In the plot of $\delta(^{137}\text{Ba}/^{136}\text{Ba})$ versus $\delta(^{135}\text{Ba}/^{136}\text{Ba})$ there is slight curvature due to increased relative production of ^{137}Ba due to production of ^{137}Cs at high neutron density followed by β^- decay. In the plot of $\delta(^{138}\text{Ba}/^{136}\text{Ba})$ versus $\delta(^{135}\text{Ba}/^{136}\text{Ba})$ curvature is more pronounced because, at the highest neutron densities corresponding to the largest ^{13}C pocket efficiencies, production of ^{135}Ba changes very little relative to production of ^{138}Ba , which increases. This is because ^{138}Ba is neutron magic ($N = 82$) and therefore has a low neutron capture cross section.

Curvature in the Ba three-isotope plots can also result from departure from the $1/\nu$ rule of the Maxwellian average cross section at 23 keV, corresponding to the average temperature when the ^{22}Ne neutron source is activated, with respect to that at 8 keV, where the neutrons are released by the ^{13}C source. For example, the ratio $\langle\sigma\nu\rangle/\nu_{\text{th}}$ of ^{134}Ba is $\sim 9\%$ greater than the corresponding ratio at 8 keV, whereas that of ^{135}Ba is $\sim 7\%$ smaller. Barium contains two s -only isotopes, ^{134}Ba and ^{136}Ba . The ratio $^{134}\text{Ba}/^{136}\text{Ba}$ could be used to determine the nature of the s -process in parent stars of these grains compared to the s -process responsible for solar system composition. Nonsolar $^{134}\text{Ba}/^{136}\text{Ba}$ ratios in data from grain aggregates have been reported (Lugaro et al. 2003a). However, in the plot of $\delta(^{134}\text{Ba}/^{136}\text{Ba})$ versus $\delta(^{135}\text{Ba}/^{136}\text{Ba})$, the error bars are large because of the relatively low abundances of ^{134}Ba and ^{135}Ba . Additionally, the branching ratio at ^{134}Cs depends on temperature (Takahashi and Yokoi 1987). From this plot it appears that the findings are consistent with predictions, but no further conclusions can be drawn. The plot of $\delta(^{137}\text{Ba}/^{136}\text{Ba})$ versus $\delta(^{135}\text{Ba}/^{136}\text{Ba})$ also shows good agreement between grain data and predictions.

All but two grains (B2-06, H4-06) fall within errors on top of the ST case for predicted values. These two are classified as uncontaminated in Fig. 4, but their 2σ uncertainties only barely overlap model predictions. Thus they may have some contamination.

The plot of $\delta(^{138}\text{Ba}/^{136}\text{Ba})$ versus $\delta(^{135}\text{Ba}/^{136}\text{Ba})$ is consistent with that of $\delta(^{137}\text{Ba}/^{136}\text{Ba})$ versus $\delta(^{135}\text{Ba}/^{136}\text{Ba})$ in that only two grains require ^{13}C pocket efficiencies below the ST case, and they are within margin of error of the D2 case. A plot of $\delta(^{138}\text{Ba}/^{136}\text{Ba})$ versus $\delta(^{137}\text{Ba}/^{136}\text{Ba})$ (not shown) indicates that grains span the same range of ^{13}C pocket efficiencies but also that the grain most depleted in ^{137}Ba and ^{138}Ba (D3-06) is not within error of predictions, which take a sharp turn upward at the ST case due to increased production of ^{138}Ba relative to ^{137}Ba . These results differ from those reported by Savina et al. (2003a), who found many cases of ^{138}Ba in grains below model predictions.

Constraining Stellar ^{13}C Pocket Efficiencies

Grains that we believe have retained their original stellar compositions require only the ST and D1.5 case ^{13}C pocket efficiencies according to the $\delta(^{94}\text{Mo}/^{96}\text{Mo})$ versus $\delta(^{92}\text{Mo}/^{96}\text{Mo})$ and $\delta(^{95}\text{Mo}/^{96}\text{Mo})$ versus $\delta(^{92}\text{Mo}/^{96}\text{Mo})$ plots in Fig. 8. Of those 19 grains, 14 fall within ST case predictions and five are within D1.5 predictions. On the $\delta(^{134}\text{Ba}/^{136}\text{Ba})$ versus $\delta(^{135}\text{Ba}/^{136}\text{Ba})$ plot it is apparent that five grains require the U1.3 case, while the remainder require ST or D1.5. The Ba data appear to require a slightly larger range of ^{13}C pocket efficiencies than the Mo data: two grains plot within error of the D2 case while the ten others are within error of D1.5 or ST. However, the two grains requiring the D2 case are the ones that very narrowly escaped exclusion on the plot of $\delta(^{96}\text{Zr}/^{94}\text{Zr})$ versus $\delta(^{135}\text{Ba}/^{136}\text{Ba})$ (Fig. 5), so it is possible they are contaminated. The greater accuracy of the Mo measurements (resulting from higher count rates and lower delta values) allows for better constraint of ^{13}C pocket efficiencies than is possible for Ba. The Zr data are more difficult to interpret given the spread in the data and predictions and the uncertainties surrounding the branch point at ^{95}Zr . Thus, this work constrains the ^{13}C pocket efficiency in the parent stars to near the ST case, which is the case in producing the solar system main component of the s -process for a star of one-half solar metallicity. These results are consistent with those of Marhas et al. (this issue) who report Ba isotopic compositions in presumably mainstream presolar SiC grains and find them, as a group, to be more s -enhanced than those analyzed by Savina et al. (2003a).

This conclusion does not mean that grains from stars with lower ^{13}C pocket efficiencies do not exist. It is possible that stars with smaller ^{13}C pockets, or those experiencing higher dredge-up and higher temperatures in thermal pulses, do not form presolar grains (Zinner et al. 2006). Additionally,

selection bias could account for those grains not being detected here. We have considered the possibility that RIMS analysis may not have the sensitivity required to measure isotopic compositions of Mo, Zr, or Ba in grains from stars with smaller ^{13}C pocket efficiencies since those grains should have lower concentrations of these elements. Of the newly synthesized s -process elements, only a fraction reach the stellar convective envelope. Third dredge-up episodes mix the s -process products as well as ^4He and ^{12}C to the surface. The envelope becomes increasingly enriched in s -process elements with each third dredge-up. The level of enrichment is described by an overproduction factor—the mass fraction of a given nuclide in the envelope divided by the mass fraction of that nuclide in the sun.

We expect presolar grains to be enriched in nuclides with high overproduction factors. Stars with smaller ^{13}C pocket efficiencies have lower overproduction factors for measured heavy elements. This should result in grains from those stars having lower concentrations of those elements. However, there is evidence that grain compositions may not be representative of stellar overproduction factors. Presolar grains with a range of Mo/Si (Kashiv 2004) and Zr/Si (Amari et al. 1995; Kashiv 2004) ratios, including some less than solar, have been measured. That finding, coupled with the observation of Mo and Zr carbide inclusions in graphite grains, indicates that the concentration of these elements in SiC grains is difficult to predict based on overproduction factors alone. However, even if significant proportions of available Mo and Zr are removed to form carbides, presolar SiC grains, on average, have larger than solar Mo/Si, Zr/Si and Ba/Si ratios (Amari et al. 1995; Kashiv 2004). Currently, there are no grains for which both isotopic compositions and elemental abundances of the same heavy element are known. (It is not possible to determine elemental concentrations using CHARISMA without additional measurements to determine the mass of sample consumed).

A model that produces a ^{13}C pocket through rotational mixing (Herwig et al. 2003) suggests that the s -process is inhibited by this mixing. However, the authors conclude that rotational mixing may play an important role in stars that are also experiencing convective overshoot, and they suggest that the spread in initial rates of mixing could result in the observed spread in the degree of s -processing indicated by observations. A recent review concludes that several phenomena may be needed simultaneously to produce the large range of ^{13}C pocket efficiencies required by previous studies (Herwig 2005).

Another study compared ratios of heavy to light s -process elements generated by models with those observed in stars (Bonačić Marinovic et al. 2006). The authors considered both extrinsic s -enhanced stars (those in binaries that are less evolved than AGB stars and with s -process elements due to mass transfer from the companion) as well as intrinsic s -enhanced stars (AGB stars producing s -process

elements). They considered a wide range of initial masses and calculated outputs for multiple thermal pulses using stellar population synthesis. Synthetic data were then weighted with the initial mass function. The improved temporal and spatial resolution over previous models allowed greater constraint of ^{13}C pocket efficiencies and indicated that a smaller range of ^{13}C pocket efficiencies—a spread of a factor of two—is needed to fit most stars in the galaxy. Thus, neither the astronomical observations nor the presolar grain data require ^{13}C pocket efficiencies beyond the range of U1.3 to D2. In fact, these two sets of observations are in complete agreement in terms of the ^{13}C pocket efficiencies they require.

Initial Stellar Compositions

Weighted linear regressions on three-isotope plots of Mo in single SiC grains have been interpreted as indicating that the initial isotopic compositions of parent stars were solar for all but one of the isotope ratios. Nicolussi et al. (1998b) interpreted the $\delta(^{100}\text{Mo}/^{96}\text{Mo})$ versus $\delta(^{92}\text{Mo}/^{96}\text{Mo})$ intercept as indicating that the initial $^{100}\text{Mo}/^{92}\text{Mo}$ ratio in parent stars had a composition different from solar. Because the present study has yielded a subset of grains that more accurately represent stellar compositions, weighted linear regression equations were calculated by the method of Williamson (1968) for uncontaminated grains only. Because of a lack of points close to the origin, the errors in the x -intercepts are too large (the smallest is $2\sigma > 700\%$) for the results to be considered meaningful. Previous studies on heavy elements in presolar grains found a high proportion of data points along lines with intercepts within error of the origin on three-isotope plots. However, the new data set contains virtually no points near the origin, making calculation of meaningful intercepts impossible and thereby precluding any conclusions about initial stellar compositions on the basis of existing data on mainstream grains.

CONCLUSIONS

Isotopic ratios of Mo, Zr, and Ba measured in mainstream SiC grains are generally consistent with model predictions for 1.5 and 3 M_{\odot} stars. However, contamination in Mo or Ba by material of solar system composition affects approximately one-third of the SiC grains from Murchison examined in this study. The source of contamination is unknown but could be related to processes on the meteorite parent body or the procedure for separation of grains from the meteorite.

When contaminated grains are removed from consideration, isotopic data for most grains require a ^{13}C pocket efficiency represented by the ST case that reproduces the solar s -process abundance in half-solar metallicity AGB stars. No grains require ^{13}C pocket efficiencies lower than that assumed for the D2 case, a factor of two smaller than the

ST one. Previous work has been unable to constrain ^{13}C pocket efficiencies because grains that were potentially contaminated were interpreted as having parent stars with ^{13}C pocket efficiencies lower than the D2 case.

Because a high proportion of SiC grains examined here show contamination, future studies of single elements in presolar grains should consider this possibility.

The uncontaminated grains come from stars whose ^{13}C pocket efficiencies are very close to the ST case. With exclusion of grains whose compositions are not representative of their parent stars, presolar grain findings do not require solar starting compositions although, for all but a few grains, they are not inconsistent with such compositions.

Acknowledgments—This work was supported by the U.S. Department of Energy Office of Science under contract no. DE-AC02-06CH11357, by the Argonne National Laboratory Graduate Fellowship program, and by the National Aeronautics and Space Administration, through grants to R. N. C., A. M. D., R. L., M. J. P., and E. Z. R. G. acknowledges the support of the Italian MIUR-FIRB project “The astrophysical origin of heavy elements beyond iron” and the Aspen Center for Physics s -process Summer School, 2005. We benefited greatly from the thoughtful reviews of L. R. Nittler, U. Ott, and an anonymous referee.

Editorial Handling—Dr. Larry Nittler

REFERENCES

- Amari S., Hoppe P., Zinner E., and Lewis R. S. 1995. Trace-element concentrations in single circumstellar silicon carbide grains from the Murchison meteorite. *Meteoritics* 30:679–693.
- Amari S., Lewis R. S., and Anders E. 1994. Interstellar grains in meteorites. I—Isolation of SiC, graphite, and diamond; size distributions of SiC and graphite. *Geochimica et Cosmochimica Acta* 58:459–470.
- Anders E. and Zinner E. 1993. Interstellar grains in primitive meteorites: Diamond, silicon carbide, and graphite. *Meteoritics* 28:490–514.
- Arlandini C., Käppeler F., Wisshak K., Gallino R., Lugaro M., Busso M., and Straniero O. 1999. Neutron capture in low-mass asymptotic giant branch stars: Cross sections and abundance signatures. *The Astrophysical Journal* 525:886–900.
- Bao Z. Y., Beer H., Käppeler F., Voss F., Wisshak K., and Rauscher T. 2000. Neutron cross sections for nucleosynthesis studies. *Atomic Data and Nuclear Data Tables* 76:70–154.
- Bernatowicz T. J., Messenger S., Pravdivtseva O., Swan P., and Walker R. M. 2003. Pristine presolar silicon carbide. *Geochimica et Cosmochimica Acta* 67:4679–4691.
- Bonačić Marinović A., Izzard R. G., Lugaro M., and Pols O. R. 2006. Population synthesis of s -process element enhanced stars: Constraining the ^{13}C efficiency. *Memorie della Società Astronomica Italiana* 77:879–884.
- Bruland K. W. and Lohan M. C. 2003. Controls of trace metals in seawater. In *The oceans and marine geochemistry*, edited by Elderfield H. Treatise on Geochemistry, vol. 6. Oxford: Elsevier-Pergamon. pp. 23–47.
- Busso M., Gallino R., Lambert D. L., Travaglio C., and Smith V. V. 2001. Nucleosynthesis and mixing on the asymptotic giant

- branch. III—Predicted and observed *s*-process abundances. *The Astrophysical Journal* 557:802–821.
- Busso M., Gallino R., and Wasserburg G. J. 1999. Nucleosynthesis in asymptotic giant branch stars: Relevance for galactic enrichment and solar system formation. *Annual Review of Astronomy and Astrophysics* 37:239–309.
- Denissenkov P. A. and Tout C. A. 2003. Partial mixing and formation of the ^{13}C pocket by internal gravity waves in asymptotic giant branch stars. *Monthly Notices of the Royal Astronomical Society* 340:722–732.
- Freytag B., Ludwig H.-G., and Steffen M. 1996. Hydrodynamical models of stellar convection—The role of overshoot in DA white dwarfs, A-type stars, and the Sun. *Astronomy and Astrophysics* 313:497–516.
- Fuchs L. H., Olsen E., and Jensen K. J. 1973. Mineralogy, mineral-chemistry, and composition of the Murchison (C2) meteorite. *Smithsonian Contributions to the Earth Sciences* 10:1–39.
- Gallino R., Arlandini C., Busso M., Lugaro M., Travaglio C., Straniero O., Chieffi A., and Limongi M. 1998a. Evolution and nucleosynthesis in low-mass asymptotic giant branch stars. II—Neutron capture and the *s*-process. *The Astrophysical Journal* 497:388–403.
- Gallino R., Lugaro M., Arlandini C., Busso M., and Straniero O. 1998b. Isotopic composition of zirconium and molybdenum in single silicon carbide presolar grains: Asymptotic giant branch model prediction and measurements (abstract). *Meteoritics & Planetary Science* 33:A54.
- Henkel T., Tizard J., and Lyon I. 2006. Comprehensive analyses of gently separated presolar SiC-grains (abstract #1700). 37th Lunar and Planetary Science Conference. CD-ROM.
- Herwig F. 2005. Evolution of asymptotic giant branch stars. *Annual Review of Astronomy and Astrophysics* 43:435–479.
- Herwig F., Blöcker T., Schönberner D., and El Eid M. 1997. Stellar evolution of low and intermediate-mass stars. IV. Hydrodynamically based overshoot and nucleosynthesis in AGB stars. *Astronomy and Astrophysics* 324:L81–L84.
- Herwig F., Langer N., and Lugaro M. 2003. The *s*-process in rotating asymptotic giant branch stars. *The Astrophysical Journal* 593:1056–1073.
- Hoppe P., Annen P., Strebel R., Eberhardt P., Gallino R., Lugaro M., Amari S., and Lewis R. S. 1997. Meteoritic silicon carbide grains with unusual Si isotopic compositions: Evidence for an origin in low-mass, low-metallicity asymptotic giant branch stars. *The Astrophysical Journal* 487:L101–L104.
- Iben I., Jr. and Renzini A. 1982. The role of semiconvection in bringing carbon to the surface of asymptotic giant branch stars of small core mass. *The Astrophysical Journal* 259:L79–L83.
- Jennings C. L., Savina M. R., Messenger S., Amari S., Nichols R. H., Jr., Pellin M. J., and Podosek F. A. 2002. Indarch SiC by TIMS, RIMS, and nanoSIMS (abstract #1833). 33rd Lunar and Planetary Science Conference. CD-ROM.
- Kashiv Y. 2004. Trace element abundances in single presolar SiC grains by synchrotron X-ray fluorescence. Ph.D. dissertation, University of Chicago, Chicago, Illinois, USA.
- Keil K. 1968. Mineralogical and chemical relationships among enstatite chondrites. *Journal of Geophysical Research* 73:6945–6976.
- Lattanzio J. C. and Lugaro M. A. 2005. What we do and do not know about the *s*-process in AGB stars. *Nuclear Physics A* 758:477c–484c.
- Lugaro M. 2005. *Stardust from meteorites: An introduction to presolar grains*. Hackensack, New Jersey: World Scientific. 209 p.
- Lugaro M., Davis A. M., Gallino R., Pellin M. J., Straniero O., and Käppeler F. 2003a. Isotopic compositions of strontium, zirconium, molybdenum, and barium in single presolar SiC grains and asymptotic giant branch stars. *The Astrophysical Journal* 593:486–508.
- Lugaro M., Herwig F., Lattanzio J. C., Gallino R., and Straniero O. 2003b. *s*-Process nucleosynthesis in asymptotic giant branch stars: A test for stellar evolution. *The Astrophysical Journal* 586:1305–1319.
- Marhas K. K., Hoppe P., and Ott U. 2007. NanoSIMS studies of Ba isotopic compositions in single presolar silicon carbide grains from AGB stars and supernovae. *Meteoritics & Planetary Science* 42. This issue.
- Merchel S., Ott U., Herrmann S., Spettel B., Faestermann T., Knie K., Korschinek G., Rugel G., and Wallner A. 2003. Presolar nanodiamonds: Faster, cleaner, and limits on platinum-HL. *Geochimica et Cosmochimica Acta* 67:4949–4960.
- Nicolussi G. K., Davis A. M., Pellin M. J., Lewis R. S., Clayton R. N., and Amari S. 1997. *s*-Process zirconium in presolar silicon carbide grains. *Science* 277:1281–1283.
- Nicolussi G. K., Pellin M. J., Davis A. M., Lewis R. S., and Clayton R. N. 1998a. Zr and Mo isotopes in single presolar graphite grains: A record of stellar nucleosynthesis (abstract #1415). 29th Lunar and Planetary Science Conference. CD-ROM.
- Nicolussi G. K., Pellin M. J., Lewis R. S., Davis A. M., Amari S., and Clayton R. N. 1998b. Molybdenum isotopic composition of individual presolar silicon carbide grains from the Murchison meteorite. *Geochimica et Cosmochimica Acta* 62:1093–1104.
- Nicolussi G. K., Pellin M. J., Lewis R. S., Davis A. M., Clayton R. N., and Amari S. 1998c. Zirconium and molybdenum in individual circumstellar graphite grains: New isotopic data on the nucleosynthesis of heavy elements. *The Astrophysical Journal* 504:492–499.
- Nicolussi G. K., Pellin M. J., Lewis R. S., Davis A. M., Clayton R. N., and Amari S. 1998d. Strontium isotopic composition in individual circumstellar silicon carbide grains: A record of *s*-process nucleosynthesis. *Physical Review Letters* 81:3583–3586.
- Savina M. R., Davis A. M., Tripa C. E., Pellin M. J., Clayton R. N., Lewis R. S., Amari S., Gallino R., and Lugaro M. 2003a. Barium isotopes in individual presolar silicon carbide grains from the Murchison meteorite. *Geochimica et Cosmochimica Acta* 67:3201–3214.
- Savina M. R., Pellin M. J., Tripa C. E., Veryovkin I. V., Calaway W. F., and Davis A. M. 2003b. Analyzing individual presolar grains with CHARISMA. *Geochimica et Cosmochimica Acta* 67:3215–3225.
- Savina M. R., Davis A. M., Tripa C. E., Pellin M. J., Gallino R., Lewis R. S., and Amari S. 2004. Extinct technetium in silicon carbide stardust grains: Implications for stellar nucleosynthesis. *Science* 303:649–652.
- Siess L., Goriely S., and Langer N. 2004. Nucleosynthesis of *s*-elements in rotating AGB stars. *Astronomy and Astrophysics* 415:1089–1097.
- Straniero O., Gallino R., and Cristallo S. 2006. *s*-Process in low mass asymptotic giant branch stars. *Nuclear Physics A* 777:311–339.
- Takahashi K. and Yokoi K. 1987. Beta-decay rates of highly ionized heavy atoms in stellar interiors. *Atomic Data and Nuclear Data Tables* 36:375–409.
- Williamson J. H. 1968. Least-squares fitting of a straight line. *Canadian Journal of Physics* 46:1845–1847.
- Zinner E. 1998. Stellar nucleosynthesis and the isotopic composition of presolar grains from primitive meteorites. *Annual Review of Earth and Planetary Sciences* 26:147–188.
- Zinner E., Nittler L. R., Gallino R., Karakas A. I., Lugaro M., Straniero O., and Lattanzio J. C. 2006. Silicon and carbon isotopic ratios in AGB stars: SiC grain data, models, and the galactic evolution of the silicon isotopes. *The Astrophysical Journal* 650:350–373.